Title

Structural pseudocapacitors with reinforced interfaces to increase multifunctional efficiency

Journal

Science Advances, 9(25)

ISSN

2375-2548

Authors

Yao, Lulu

Zheng, Kai

Koripally, Nandu

et al.

Publication Date

2023-06-23

DOI

10.1126/sciadv.adh0069

APPLIED SCIENCES AND ENGINEERING

Structural pseudocapacitors with reinforced interfaces to increase multifunctional efficiency

Lulu Yao[1], Kai Zheng[2], Nandu Koripally[2], Naresh Eedugurala[3], Jason D. Azoulay[3,4], Xinyu Zhang[2], Tse Nga Ng[1,2]*

Structural supercapacitors hold promise to expand the energy capacity of a system by integrating load-bearing and energy-storage functions in a multifunctional structure, resulting in weight savings and safety improvements. Here, we develop strategies based on interfacial engineering to advance multifunctional efficiency. The structural electrodes were reinforced by coating carbon-fiber weaves with a uniquely stable conjugated redox polymer and reduced graphene oxide that raised pseudocapacitive capacitance and tensile strength. The solid polymer electrolyte was tuned to a gradient configuration, where it facilitated high ionic conductivity at the electrode-electrolyte interfaces and transitioned to a composition with high mechanical strength in the bulk for load support. The gradient design enabled the multilayer structural supercapacitors to reach state-of-the-art performance matching the level of monofunctional supercapacitors. In situ electrochemical-mechanical measurements established the device durability under mechanical loads. The structural supercapacitor was made into the hull of a model boat to demonstrate its multifunctionality.

INTRODUCTION

Today's electrochemical storage devices are restricted in capacity, a key challenge that limits the operational time of wireless devices and invokes range anxiety in the electric transportation sector. To increase the storage capacity, one approach is to leverage structural volume to create structural batteries/supercapacitors (*1*–*8*), in which energy storage is integrated with load-bearing functions and thus facilitates mass and weight savings. For example, carbon fibers (CFs) used for structural reinforcements also exhibit good conductivity. So, in multifunctional structures, CFs can serve as electrode scaffolds with surface modification or added active materials, and then the electrodes are stacked with separators and solid-state electrolytes to complete an electrochemical cell. This layered configuration is similar to high-strength laminates and incorporates both electrochemical and mechanical functions, which are attractive to aviation and maritime industries where structural composites are already prevalent (*9*–*11*). However, when comparing the multifunctional composites to their monofunctional counterparts, there are additional challenges with conflicting requirements between electrochemical functions and mechanical properties.

Here, we develop strategies based on interfacial engineering to decouple the trade-offs and concurrently improve energy storage and mechanical strength in structural supercapacitors. Supercapacitors offer much longer cycle life than batteries and are conducive to durable operation, which is advantageous in scenarios where the structures are integrated and not frequently replaced. Yet the energy and power densities of structural supercapacitors have been substantially lower than monofunctional devices due to shortcomings in the current implementation of structural electrodes and electrolytes.

First, for structural electrodes, the limitation stems from the trade-off between mechanical strength and specific capacitance. To increase the electric double layer capacitance, CF electrodes were treated by chemical activation processes at high temperature, but the treatment reduced structural strength due to damaged fibers (*12*). Alternatively, the surface of CFs was modified by carbon aerogel (*13*) or metal oxide (*14*), although these electronic materials did not contribute to mechanical reinforcement.

Second, for the structural electrolyte, previous designs have suffered from low ionic conductivity that leads to loss of energy and power density as charge exchange sites were inaccessible. The ionic conductivity is typically inversely proportional to the mechanical modulus of the composite (*15*, *16*). Cross-linked epoxy resins are one of the most widely used matrices for laminates and have been blended with ionic-liquid salts to form phase-segregated electrolytes (*17*), although their mechanical moduli were drastically diminished due to disruptions to cross-linking. Meanwhile, epoxy matrices with low salt content showed better mechanical properties but low ionic conductivity. While silica or alumina fillers (*18*–*20*) were added to increase ion diffusion paths (*21*), the improvements were incremental and the low ionic conductivity was still severely limiting the kinetics in structural supercapacitors, resulting in peak power that was an order of magnitude less than typical monofunctional devices (*3*).

To overcome the bottlenecks in structural supercapacitors, this work focuses on the crucial interfaces of electrodes and electrolyte as illustrated in Fig. 1. For the structural electrode, the CFs are conformally coated with a stable conjugated redox polymer (*22*, *23*) that contributes Faradaic charge storage with a large 3-V potential window and raises the specific capacitance substantially compared to prior electrodes. In addition to favorable electronic properties, the redox polymer enhances mechanical moduli of the composite (*24*) on account of its sulfur-containing moieties that can form hydrogen bonds or react with cross-linkers in the electrolyte. The

[1]Materials Science Engineering Program, University of California San Diego, La Jolla, CA 92093, USA. [2]Department of Electrical and Computer Engineering, University of California San Diego, La Jolla, CA 92093, USA. [3]School of Polymer Science and Engineering, University of Southern Mississippi, 118 College Drive #5050, Hattiesburg, MS 39406, USA. [4]School of Chemistry and Biochemistry, School of Materials Science and Engineering, Georgia Institute of Technology, Atlanta, GA 30332, USA.
*Corresponding author. Email: tnn046@ucsd.edu

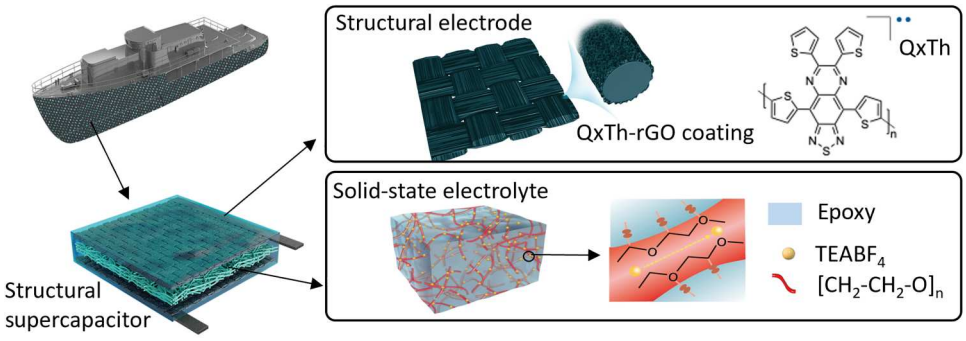

Fig. 1. Schematics of our structural supercapacitor. The redox polymer coating QxTh-rGO on CFs increases gravimetric capacitance of the electrodes. An ion-percolation network in the epoxy matrix offers high ionic conductivity and mechanical strength in the functionally graded electrolyte.

structural electrolyte is based on an epoxy matrix improved with polyethylene oxide (PEO) (*25*, *26*), which provides percolation conduits for ion transport while maintaining mechanical strength much better than ionic-liquid channels in prior phase-segregated electrolytes.

A key design in this work leverages a gradient composition in the electrolyte to increase the kinetics at the electrode-electrolyte interfaces and push up the power density considerably in structural supercapacitors to be on par with monofunctional devices. The gradient electrolyte is tuned such that the regions immediately next to electrodes incorporate a higher concentration of ion-conducting PEO to increase access to the electrolyte salts and promote fast kinetics, whereas the middle region contains a lower concentration of PEO in the epoxy matrix to better support load transfer while still maintaining ion percolation. The performance of structural supercapacitors with uniform or gradient electrolyte is assessed to investigate how the structural adjustments affect power and energy density, cycling stability, and overall mechanical properties including tensile and flexural stress under deformation. The combined electrochemical and mechanical performance is evaluated through a metric of multifunctional efficiency for comparison with state-of-the-art devices.

Last, as a feasibility study, we fabricate a structural supercapacitor to serve as the hull of a model boat. The boat is integrated with a solar panel for charging up the supercapacitor hull, which in turn powers up the boat motor to cruise across a pool. This demonstration shows the potential of structural supercapacitors to facilitate mass savings and increase the capacity for energy harvesting and storage in future electric systems.

RESULTS AND DISCUSSION

Structural electrodes

The structural electrodes were made from a CF fabric modified by a coating of an open-shell conjugated redox polymer and reduced graphene oxide (rGO). The coating was prepared by electrodeposition, in which a solution mixture of rGO and monomer 4,6,7,9-tetra(thiophen-2-yl)-[1,2,5]thiadiazolo[3,4-*g*]quinoxaline (QxTh) was drop-casted onto the CF fabric and reacted by cathodic electropolymerization (processing details included in the "Experimental procedures" section and in fig. S1) to form the pseudocapacitive coating. The redox polymer QxTh was selected because of its high specific capacitance (297.6 F g^{-1}) and stability over a wide potential window of 3 V due to its open-shell characteristics (*22*), and rGO was incorporated to enhance the conductivity and porosity of the coating. As seen in the scanning electron microscopy (SEM) images, the surface of the pristine CF was smooth in Fig. 2A; then, after the polymerization process, a porous QxTh-rGO coating was conformally deposited on the CF in Fig. 2B. The porosity was beneficial for the transport of counter ions and tolerant to dimensional changes upon redox cycling.

From cyclic voltammetry (CV) measurements, Fig. 2C presents the gravimetric capacitance of the pristine and QxTh-rGO coated CF electrodes. Accounting for the weight of the CF (12.07 mg per 1 cm^2 electrode area), the pristine CF electrode showed a capacitance of 0.16 F g^{-1}, while the QxTh-rGO@CF electrode reached 65.2 F g^{-1} when characterized as an anode (in the voltage range of −0.5 to −2 V versus Ag/Ag^+ reference), and 34.6 F g^{-1} as a cathode (−0.5 to 1 V versus Ag/Ag^+) in Fig. 2D. A coating of 3-mg QxTh-rGO on 9.93-mg CF increased the electrode gravimetric capacitance by up to 400-fold compared to CF alone (supporting measurements in fig. S2 and table S1). The specific capacitance can be raised further by depositing more QxTh-rGO onto the CF surface.

The energy storage mechanism of QxTh-rGO was also studied through Augustyn-Simon-Dunn analysis (*27*). In this method, the current i and the scan rate υ of CV is expressed as $i = i_c + i_d = k_1\nu + k_2\nu^{0.5}$, or equivalently $\frac{i}{\nu^{0.5}} = k_1\nu^{0.5} + k_2$ (*28*, *29*), where k_1 is the capacitive constant (related to the electric double layer formation), k_2 is the diffusion-controlled constant (related to redox reactions), and ν is the scan rate. A set of CV data measured at various scan rates were obtained and plotted as $i/\nu^{0.5}$ versus $\nu^{0.5}$ in fig. S3. In the QxTh-rGO supercapacitor, the contribution of capacitive EDL storage was 50% at a slow scan rate of 1 mVs^{-1} and increased to 73% with a faster scan rate of 7 mVs^{-1}. In galvanostatic charge-discharge tests, the QxTh-rGO@CF electrode exhibited capacity retention of 96.1% as an anode and 97.5% as a cathode after 10,000 full charge/discharge cycles (fig. S4). This retention result indicates great redox stability of QxTh due to the extended delocalization of charge density within this open-shell conjugated polymer.

In addition to the excellent electrochemical performance, the QxTh-rGO coating provided additional mechanical reinforcement to the structural electrode. In Fig. 2E, the maximum tensile strength (stress-to-failure point) was 4.5 GPa for QxTh-rGO@CF, slightly better than pristine CF at 4.3 GPa. The tensile modulus was 103 GPa for QxTh-rGO@CF, also higher than the CF modulus of 84

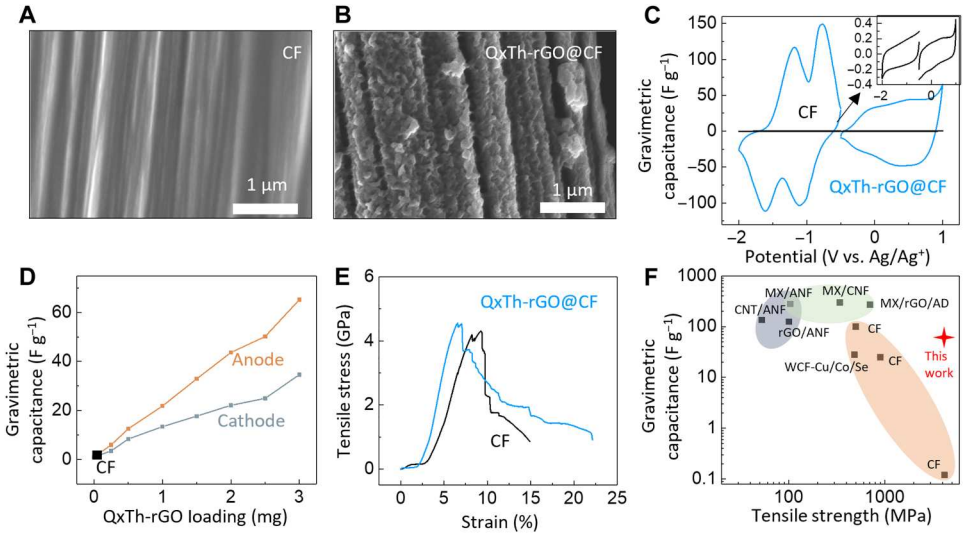

Fig. 2. Characterization of structural electrodes. SEM images of (**A**) pristine CFs and (**B**) CFs coated with QxTh-rGO. (**C**) Gravimetric capacitance extracted from CV at a scan rate of 10 mV s^{-1}. The QxTh-rGO sample is at 3-mg cm^{-2} loading. The inset zooms in on the data for CFs. (**D**) Gravimetric capacitance as a function of QxTh-rGO loading on the CF. The capacitance was calculated based on CV data collected at 10 mV s^{-1} in a 0.5 M $TEABF_4$/PC electrolyte. (**E**) Tensile stress versus applied strain for the pristine and modified CF samples. (**F**) Comparison of gravimetric capacitance and tensile strength of structural electrodes: carbon fiber (CF) (*42*), rGO/aramid nanofiber (ANF) (*42*), carbon nanotube (CNT)/ANF (*43*), MXene (MX)/ANF (*44*), MX/cellulose nanofibrils (CNFs) (*45*), MX/rGO/AD (*46*), and woven CF (WCF)–Cu/Co/Se. (*47*).

GPa. This higher mechanical performance was attributed to the polymer acting as a binder for CFs (*26*). After tensile strain tests, SEM images showed that QxTh-rGO was still conformally coated on the strained fibers (fig. S4), confirming the strong adhesion of the polymer coating, superior to particulate pseudocapacitive materials (*14*) that had issues with long-term adhesion to CF.

Among state-of-the-art structural electrodes in Fig. 2F, QxTh-rGO@CF offered the highest tensile strength, as the facile processing at room temperature did not damage the CF and retained the inherent structural organization that imparted robust mechanical properties to CF weaves. While the specific capacitance of our electrodes was not the highest in the comparison chart of Fig. 2F, the other materials showed an order of magnitude lower tensile strength and moduli and were further limited in their operational voltage window *V*. As summarized in table S2, the composites of MXene or aramid nanofibers were limited to a potential window below 1 V compared to the stability window of 3 V in QxTh-rGO@CF. Since energy density *E* is proportional to $E = 0.5\ CV^2$, at a given capacitance *C*, the approach of expanding the potential window from 1 to 3 V would offer a ninefold increase in energy density.

Structural electrolyte

For multifunctional laminates, the solid-state electrolyte plays key roles in ions conduction and load bearing, to achieve inherently more resilient and safer devices than conventional liquid/gel electrolytes when subjected to mechanical loads. Here, we chose epoxy resin as the base for our solid polymer electrolyte and adjusted its composition in terms of electrolyte salt concentration, ion percolation agent PEO, and functionally graded configuration (*30*) to maximize the electrochemical and mechanical performance of the composite. The epoxy provided cross-linked bonds at interfaces to strongly bind the electrode and separator components together for high strength. The addition of ion-conducting polymer PEO created diffusion channels as a percolation network through the epoxy matrix, allowing us to replace expensive ionic-liquid salts in previous phase-segregated channel designs (*17*) with tetraethylammonium tetrafluoroborate ($TEABF_4$) salts that are less expensive compared to ionic liquids. As a common binder (*25*), PEO would cross-link with epoxy to maintain mechanical modulus and would certainly be stronger as a solid than ionic-liquid channels and unaffected by aggregation problems like mesoscopic inorganic fillers, while enhancing ionic conductivity of the solid polymer electrolyte.

Our study of electrolyte composition is displayed in Fig. 3A, for which we categorized the results into four groups. The salt and PEO ratios (wt %) were calculated from the weight of the respective component divided by the total weight ($TEABF_4$ salt + PEO + epoxy resin). Electrochemical impedance data used to calculate the ionic conductivities are shown in fig. S6 and table S3. For epoxy mixed with electrolyte salts only, the electrolyte ions were not able to diffuse in the cross-linked resin, and the ionic conductivity was very low >0.04 mS cm^{-1} [type (i) in gray color]. Upon adding PEO to the resin, ion diffusion along PEO improved transport and raised the ionic conductivity to 0.14 mS cm^{-1} [type (ii) in green]. If more salt was added per PEO amount, the ionic conductivity was increased further and reached up to 0.4 mS cm^{-1} [type (iii) in blue]. However, increasing the salt ratio beyond 20 wt % affected processing and mechanical performance, because the $TEABF_4$ salts were dissolved in a propylene carbonate solvent which slowed down the cross-linking reaction in the epoxy, and the residual solvent decreased the mechanical strength. Meanwhile, increasing the PEO ratio [type (iv) in orange] has a similar effect of reducing mechanical moduli because of the low rigidity of PEO. Then, for device fabrication, we used a combination of two electrolyte compositions, denoted by the blue [18 wt % salt and 9 wt % PEO; labeled as (iii)] and green [5 wt % salt and 10 wt % PEO; labeled as (ii) open circles in Fig. 3A, to construct a functionally graded electrolyte.

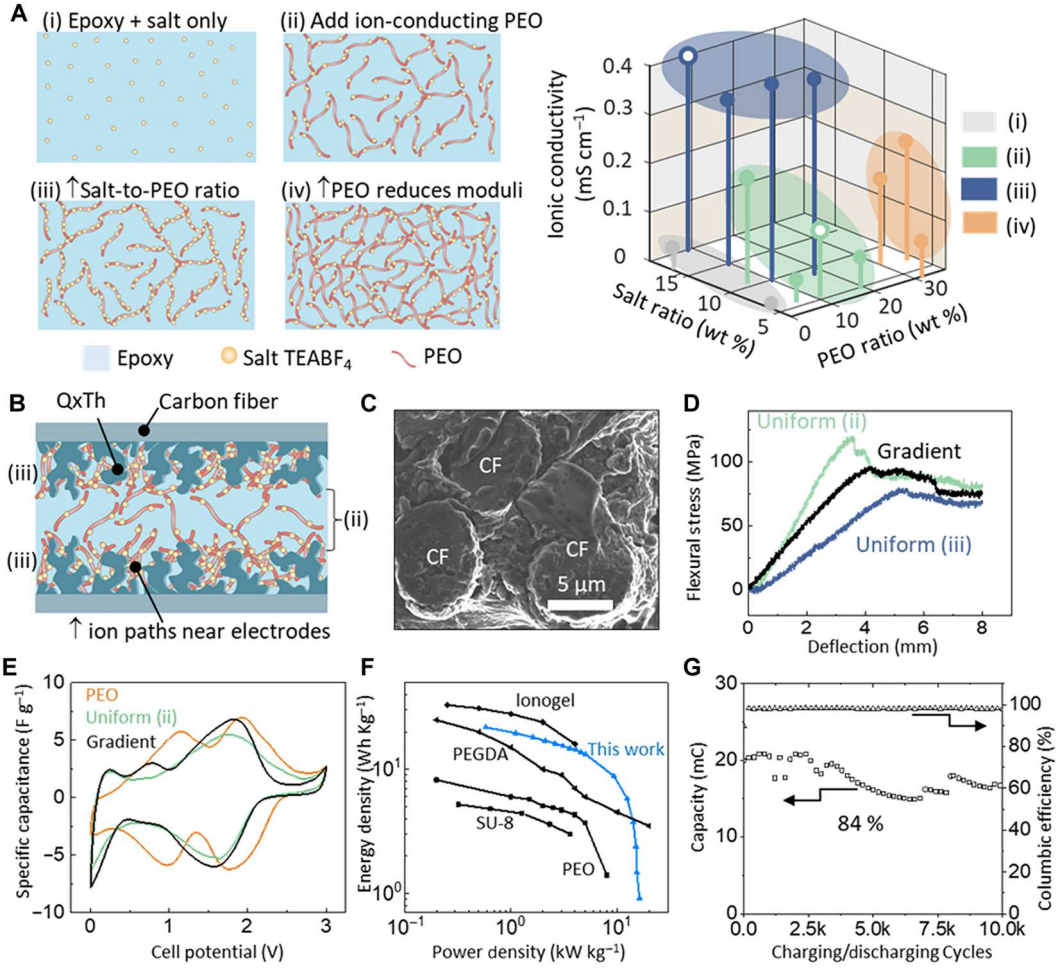

Fig. 3. Characterization of structural electrolytes and supercapacitors. (**A**) Schematics and measurements of ionic conductivity as the electrolyte composition was varied to different salt:PEO:epoxy ratios. (**B**) A cross-sectional schematic of the electrolyte with a gradient composition in which regions near electrodes had higher concentration of salt and PEO than in the middle to improve device kinetics. (**C**) SEM image of the solid polymer electrolyte infiltrating around the CF electrode. (**D**) Flexural stress versus deflection on samples with uniform (ii), uniform (iii), or the gradient electrolyte. The uniform electrolyte compositions (ii) and (iii) correspond to the green and blue open circles in (A), respectively. (**E**) CV at a scan rate of 1 mV s^{-1} on structural supercapacitors with different polymer electrolytes. (**F**) Comparison of energy and power densities in state-of-the-art supercapacitors using solid-state electrolytes: this work using the gradient electrolyte, ionogel (*48*), polyethylene glycol diacrylate (PEGDA) (*49*), PEO (*50*), and SU-8 (*51*). (**G**) Capacitance retention and coulombic efficiency of the structural supercapacitor with the gradient electrolyte under full charge-discharge cycles of 3 V at a current density of 2 mA cm^{-2}. Fluctuations near 7000 and 8000 cycles were due to the electrode contacts being resecured.

Integrated structural supercapacitor

Electrochemical characterization

In structural supercapacitors, the electrolyte was typically a uniform composite directed by vacuum infusion to flow through the electrodes and separator and then solidified together. The epoxy resin is essential to maintain rigidity for load support, but it is electrochemically inert and limits surface adsorption and interfacial redox reactions that dictate the cell capacitance and energy storage capacity. Instead of a uniform electrolyte, we designed structural supercapacitors with a functionally graded electrolyte illustrated in Fig. 3B to improve ion exchange at the electrolyte-electrode interfaces. For the functionally graded (namely, gradient) structure, the electrodes were coated with an electrolyte with a high salt ratio, more specifically, of the composition indicated by the blue open circle [labeled as (iii) in Fig. 3A]. This choice facilitated ion access to electrode surfaces and was favorable for capacitance; however, the high salt ratio compromised the mechanical properties of the epoxy. Hence, to balance mechanical and electrochemical performance, the middle region of the electrolyte (where the separator was embedded) used the composition with a low salt ratio as indicated by the green open circle [type (ii)], which still retained sufficient ion percolation network while offering high mechanical strength. The different electrolytes were stencil-printed onto the electrodes or separator, partially cured, and then hot-pressed together to complete curing. The solid polymer electrolyte penetrated into and enclosed the electrodes very well to ensure intimate contact, as seen in the SEM image in Fig. 3C.

Figure 3D compares the flexural properties of different electrolytes. The uniform (ii) electrolyte showed a high flexural strength of 130 MPa, but its ionic conductivity was only 0.14 mS cm^{-1}. In contrast, the uniform (iii) electrolyte was lower in flexural strength at 75 MPa while higher in ionic conductivity at 0.4 mS cm^{-1}. The

gradient electrolyte combined the two compositions and attained a flexural strength of 91 MPa, while maintaining a high ionic conductivity of 0.4 mS cm^{-1}. Thus, the gradient design gained the benefits of increased mechanical strength without sacrificing electrochemical performance.

Figure 3E presents the electrochemical characteristics of three devices, comparing the above gradient electrolyte, a uniform (ii) electrolyte, and a nonstructural PEO electrolyte without epoxy. The electrolyte with no epoxy and solely PEO (orange curve, salt:PEO at 33 wt %) can be considered as an upper bound for the electrochemical performance in solid polymer electrolytes, but it is monofunctional and cannot support load-bearing functions because PEO will deform easily on account of its low mechanical moduli. The uniform (ii) electrolyte was composed of a PEO-epoxy resin with a low salt ratio, and the associated device (green curve) exhibited the lowest specific capacitance among the three structures and only one redox peak in the CV data as opposed to two peaks in the other devices, indicating slow kinetics due to low ionic conductivity. The gradient electrolyte (black curve) improved the interfacial kinetics and increased the device specific capacitance by ~10% across all scan rates when compared to the uniform electrolyte (Fig. 3E and fig. S7).

Overall, our multifunctional supercapacitor with the gradient electrolyte was comparable to devices with monofunctional gel electrolytes, providing power and energy densities in similar orders of magnitude in Fig. 3F. One reason for the high performance is that our device used pseudocapacitive QxTh-rGO@CF electrodes that did not rely as much on interfacial porosity and ionic rearrangement as electric double layer (EDL) electrodes, making our design favorable for pairing with solid electrolytes. Our redox electrode operating with the gradient electrolyte retained 83% of capacitance in comparison to its operation in a liquid electrolyte. In contrast, an EDL activated-carbon device with a solid electrolyte retained only 15% of capacitance, as shown in fig. S8. Here, the redox electrode and gradient electrolyte design promoted fast kinetics to achieve power densities on the level of typical monofunctional supercapacitors, and this is exciting for removing the major drawback of low power outputs in structural supercapacitors.

The stability of the structural supercapacitor with the gradient electrolyte was excellent with >99% coulombic efficiency and 84% capacity retention after 10,000 full charge-discharge cycles over a wide potential window of 3 V (Fig. 3G). The cycle life of our device was comparable or better than state-of-the-art structural supercapacitors as listed in table S4. The self-discharge characteristics of our structural supercapacitor was slightly better than a commercial supercapacitor (1 F, 2.7 V, DRL 105S0TF12RRDAP, Samxon Supercap PoiLee), with a 1-V decrease after 10 hours (fig. S8E) because of the decreased side reactions (*31*, *32*) in solid electrolytes.

Mechanical characterization

The mechanical properties of the structural supercapacitor with the gradient electrolyte were compared to two monofunctional structures, in which one laminate was bonded by epoxy only (maximum mechanical strength but no electrochemical function) and the other was with the PEO electrolyte (maximum ionic conductivity but low structural rigidity). These samples had two layers of QxTh-rGO@CF fabric and a cellulose separator sandwiched in between. The weak binding strength of PEO led to separation of the layers at 2.1 MPa when the structure was placed under tensile strain. The gradient structural supercapacitor remained intact up to the tensile stress of 167 MPa, and the epoxy laminate sustained 255 MPa before failure, as seen in Fig. 4A. The tensile modulus, namely, the slope of tensile stress versus applied strain, was 10.2 GPa for the structural supercapacitor.

In Fig. 4B, the flexural properties were measured by a three-point bending setup that applied deflection to determine stiffness. The PEO device was flexible and showed flexural stress <20 MPa. In contrast, the flexural strength was 91 MPa for the gradient structural supercapacitor and 275 MPa for the epoxy laminate when the structures reached permanent deformation. This high flexural strength is higher than the typical CF based structural supercapacitor (*33*), although slightly worse than the device with special honeycomb core separator design which is more difficult to fabricate (*34*). For visual comparisons, the photographs in Fig. 4C showed the stiffness of each sample with a thickness of 0.8 mm, where the PEO structure was severely bent under a 20-g weight, and the gradient electrolyte was able to support a 100-g weight, potentially strong enough as structural materials in electronic casings and internal parts of electric vehicles (*9*–*11*). Since practical applications might require thick carbon-fiber reinforced composites, we have also measured the flexural stress of structural supercapacitors integrated with multiple layers of CFs (eight electrodes with seven separators) and observed that the flexural modulus was maintained (fig. S9). Therefore, it would be feasible to scale up and adapt the layered composites for different target thicknesses according to the desired use case.

Multifunctional efficiency

Simultaneous monitoring of electrochemical and mechanical characteristics were carried out on the structural supercapacitor with the gradient electrolyte. An example was the CV measurements as a function of applied deflection shown in Fig. 4D. From the current-voltage characteristics, the extracted capacitance was 47.1 mF in the initial flat state and 40 mF at 7-mm deflection, and thus the device retained 85% of its original capacitance even under large deformation. Figure 4E summarizes the series of in situ measurements that concurrently tracked flexural stress and capacitance as the structural supercapacitor was subjected to increasing deflection. When the structural deflection was less than 3 mm, the device capacitance remained constant, and only when the deflection was 3 mm and beyond that the capacitance started to decrease and leveling off to 85% of the initial capacitance as the structure reached its peak flexural stress after which it was irreversibly deformed. The characterization here indicated stable electrode-electrolyte interfaces in our structural supercapacitor to maintain electrochemical and mechanical performance as external mechanical loads were applied.

Figure 5A presents the energy and power densities of state-of-the-art structural supercapacitors and batteries in comparison to our devices. While batteries are generally expected to have higher energy density than supercapacitors, our structural supercapacitor exceeded the energy density of the $Fe(OH)_2$ structural battery (*35*) and achieved much larger power density than all the other structural energy storage devices. Our device metrics were calculated with the total device mass including electrodes, separator, and electrolyte, as explained in the "Experimental procedures" section. We fabricated three device structures: one with two electrode layers (2L), another with nine electrode layers (9L), and a third device with nine electrode layers and a higher loading of QxTh-rGO (H-9L). The 2L device was a basic structure with QxTh-rGO deposited on a

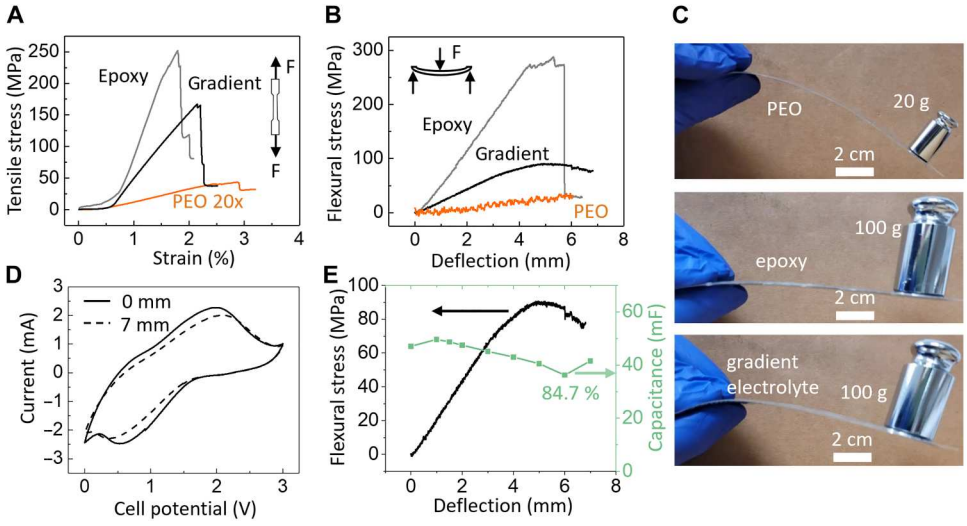

Fig. 4. Mechanical properties of structural supercapacitors. (**A**) Tensile stress versus applied strain for laminates bonded by different polymers. Gray: epoxy only with no electrolyte salt. Black: gradient electrolyte same as in Fig. 3B. Orange: PEO with salt:PEO at 33 wt %, same as the orange data in Fig. 3E. For the stress measurement, the sample cross-sectional area was 0.58 mm by 2 cm and the length was 5 cm. (**B**) Flexural strength versus deflection distance. The device dimensions were 10 cm by 1 cm by 0.58 mm. (**C**) Photographs showing the deflection of laminates under weights. The film thickness was 0.8 mm including encapsulation PET films. (**D**) CV at 20 mV s^{-1} of the structural supercapacitor with the gradient electrolyte, taken under the flexural deformation of 0- or 7-mm deflection. (**E**) Flexural stress and capacitance as a function of deflection distance, measured on the structural supercapacitor with the gradient electrolyte.

single side of each CF layer. It was able to provide 0.0575 Wh kg^{-1} at 1019 W kg^{-1} power density. However, considering that the CF substrate contributed a large portion of the electrode mass but little capacitance, there was room to improve the device design by depositing the high-capacitance QxTh-rGO on both sides of each CF and stacking the anodes and cathodes as shown in fig. S10 to minimize the CF mass. This arrangement was used in the 9L device, which theoretically would have a charge-storage capacity equivalent to 8× 2L devices while eliminating the mass of seven CF substrates. Thus, the gravimetric energy density may increase by 1.78-fold (=16/9) for the 9L device compared to the 2L device.

The measurements in Fig. 5A showed higher energy densities for the 9L device than the 2L one, although the power output was comparatively decreased for the 9L structure, probably due to a small resistance increase introduced by stacking electrode current collectors. For the third device labeled H-9L, we roughly doubled the QxTh-rGO loading on each CF substrate compared to the 9L device. The H-9L device showed a lower power density than 9L device because of the slower kinetics from the thicker QxTh-rGO coating. Nonetheless, the H-9L device still offered power density within the same order of magnitude as monofunctional supercapacitors. When delivering at a high power of 584.7 W kg^{-1}, our H-9L device supplied an energy density of 0.2096 Wh kg^{-1}. The maximum energy density was 2.443 Wh kg^{-1} at a power of 17.8 W kg^{-1}, which matched the level of monofunctional supercapacitors and made it competitive against commercial devices.

To quantify the potential advantages of multifunctional structures over monofunctional counterparts, there have been different approaches (*36*–*38*) to combine the structural and electrochemical properties and tie them into a multifunctional efficiency metric η_{multi} defined as

$$\eta_{multi} \equiv \eta_E + \eta_M = \frac{E_{multi}}{E_{typ}} + \frac{M_{multi}}{M_{typ}}$$

where η_E and η_M are the electrochemical or mechanical efficiency, respectively, and each of them is computed by comparing the specific electrochemical properties E_{multi} (such as energy and power, etc.) or specific mechanical properties M_{multi} (such as strength, stiffness, toughness, etc.) of the multifunctional laminate relative to baseline values E_{typ} or M_{typ} from typical monofunctional structures. If η_{multi} is greater than 1, then it indicates weight savings over conventional systems of using independent monofunctional components. In the analysis in Table 1, we simplified Eq. 1 to consider only energy density for η_E and only tensile modulus for η_M. One of the reasons we simplified Eq. 1 to use only tensile modulus is because of limited mechanical data in other reports. While this may be oversimplifying, it provided a useful perspective for materials comparison. It is worth noting that Eq. 1 as written assigns an equal weight (50% each) to the roles of structural support and energy storage. If in future systems, those roles are not equally important, then the multifunctional efficiency can be adjusted by assigning different scaling factors to each property (*37*).

Regarding the benefit of multifunctionality, we compared our device to state-of-the-art structural supercapacitors listed in Table 1, where the efficiency metrics were calculated on the basis of the baseline values of E_{typ} = 2.5 Wh kg^{-1} for energy density (*3*) and M_{typ} = 31.5 GPa for tensile modulus (*2*) from monofunctional standards. Other parameters of structural supercapacitors are summarized in table S4. Since η_E and η_M are ratios and by definition dependent on the denominator values and yet there are no consistent baseline values across publications, we normalized the prior works in Table 1 with the common baseline values chosen here to be fair in the analysis.

Table 1. Energy density and tensile modulus of state-of-the-art structural supercapacitors. The efficiency η_E was calculated with E_{typ} = 2.5 Wh kg^{-1} and η_M with M_{typ} = 31.5 GPa. The letter labels correspond to those in Fig. 4B. VG, vertical graphene; PANI, polyaniline; CAG, carbon aerogel.

Electrode materials (reference) (label)	Energy density (Wh kg^{-1})	Tensile modulus (GPa)	η_E	η_M	η_{multi}
2L QxTh-rGO-CF (this work)	1.369		0.548		0.872
9L QxTh-rGO-CF (this work)	1.823	10.2	0.729	0.324	1.053
H-9L QxTh-rGO-CF (this work)	2.443		0.977		1.301
CF-ZnO (*14*) (a)	1.562	21	0.062	0.667	0.729
CF-VG-MnO_2 (*54*) (b)	0.0122	4.313	0.0049	0.137	0.142
PANI-CF (*55*) (c)	0.0494	0.907	0.020	0.0288	0.0485
Graphene-CF (*56*) (d)	6.6×10^{-5}	20.72	2.66×10^{-5}	0.658	0.658
CAG-CF (*57*) (e)	0.093	32.9	0.037	1.045	1.082

The η_E of our structural supercapacitors with gradient electrolyte was 0.548 for the 2L device, 0.729 for 9L, and reached 0.977 for the H-9L device, the highest among the structures in Table 1. This high η_E was attributed to the high gravimetric capacitance of our electrode, the good ionic conductivity from the gradient electrolyte, and the multilayer stacking configuration for mass savings. Here, the stacking configuration with double-sided coating for each current collector has been used in monofunctional batteries, which motivated us to try such designs for structural supercapacitors. The η_M of our devices was 0.324 with the epoxy-reinforced design. The tensile modulus was measured for the 2L device, and we assume it to remain the same for multilayer configurations, as shown in fig. S9. The total η_{multi} was found to be 1.053 for the 9L device and 1.301 for H-9L, meaning that our structural supercapacitors would offer a weight-saving advantage and provided the highest multifunctional efficiency to the best of our knowledge. Also, please note that in Fig. 5B all the prior works were clustered in the region with very low electrochemical efficiency η_E. Our structural supercapacitor designs with η_E up to 0.977 were in the region with high electrochemical efficiency. Thus, while our devices would offer structural support with decent mechanical efficiency η_M, they contribute more heavily to electrochemical functions and η_E. This unique position would be complementary to prior structural supercapacitors and well-suited for applications in which energy capacity is very critical to their missions.

Prototype based on the structural supercapacitor: Electric boat powered by an energy-harvesting system

After device characterization, our structural supercapacitor design was applied in a proof-of-concept demonstration. Motivated by the pervasive use of carbon-fiber laminates in boat building, we fabricated a model boat for which the entire hull was consisted of structural supercapacitors serving dual functions of structural support and energy storage for powering the boat motor in Fig. 5C. The boat-hull supercapacitor was integrated into an energy-harvesting system with a solar cell that was as the sole energy input for the boat. A control circuit automatically toggled the connections of the supercapacitor to be charged by the solar cell or to be discharged to power the boat motor. Upon power on, the control circuit would be in the charging mode until the supercapacitor reached the threshold voltage of 2.1 V. Once the supercapacitor voltage exceeded the set threshold, the control circuit switched to the discharging mode, in which the supercapacitor sent current to turn on the motor, and the boat cruised over water as seen in the movie S1. When the supercapacitor voltage dropped to 0.1 V, the control circuit switched back to be in charging mode, and the charging/discharging process would repeat as seen in Fig. 5D till the circuit was turned off. The capacitance of the boat-hull supercapacitor was 2.72 F; it allowed 1.9 min of motor run time after 4.8 min of charging under the mid-afternoon sun. For the operational voltage between 0.1 and 2.1 V, the structural supercapacitor was tested for 35,000 charge-discharge cycles and retained 83% of its initial capacity, demonstrating excellent stability and long cycle life. This demonstration shows the supercapacitor capable of meeting the structural and energy storage requirements of an autonomous energy-harvesting system operating in aquatic environments.

This work presents a design for structural supercapacitors to overcome the bottlenecks at electrode and electrolyte interfaces. The electrode coating of pseudocapacitive QxTh-rGO with a wide potential window of 3 V substantially raised the gravimetric energy and power densities, and the conjugated polymer strengthened the electrode tensile properties better than particulate materials with weaker adhesion to CFs. The electrolyte was reinforced by solid PEO to maintain ion percolation without resorting to liquid ion channels, and the epoxy-PEO-$TEABF_4$ resin was optimized to be functionally graded from the electrode to the separator interfaces, transitioning from a composition with high ionic conductivity near the electrodes to one with high mechanical strength at the separator for load transfer. This gradient configuration would be useful for others working on nonflammable solid electrolytes to enhance the device performance and safety.

Here, the structural supercapacitors were shown to achieve state-of-the-art performance with an energy density of 2.443 Wh kg^{-1} at the power output of 17.8 W kg^{-1} and a tensile modulus of 10.2 GPa. The gradient design pushed the maximum power density (1019 W kg^{-1}) into the same range as monofunctional supercapacitors, an important milestone for structural energy storage devices. The in-situ mechanical-electromechanical measurements established the device durability under mechanical loads, as the structure retained 85% capacitance at 80-MPa flexural stress. The flexural strength of 91 MPa and tensile strength of 167 MPa are sufficient for many electronic housings. After 10,000 full charge-discharge cycles over 3 V, the capacity retention was 84%, and such long cycle life ensures that structural parts would not need to be replaced frequently.

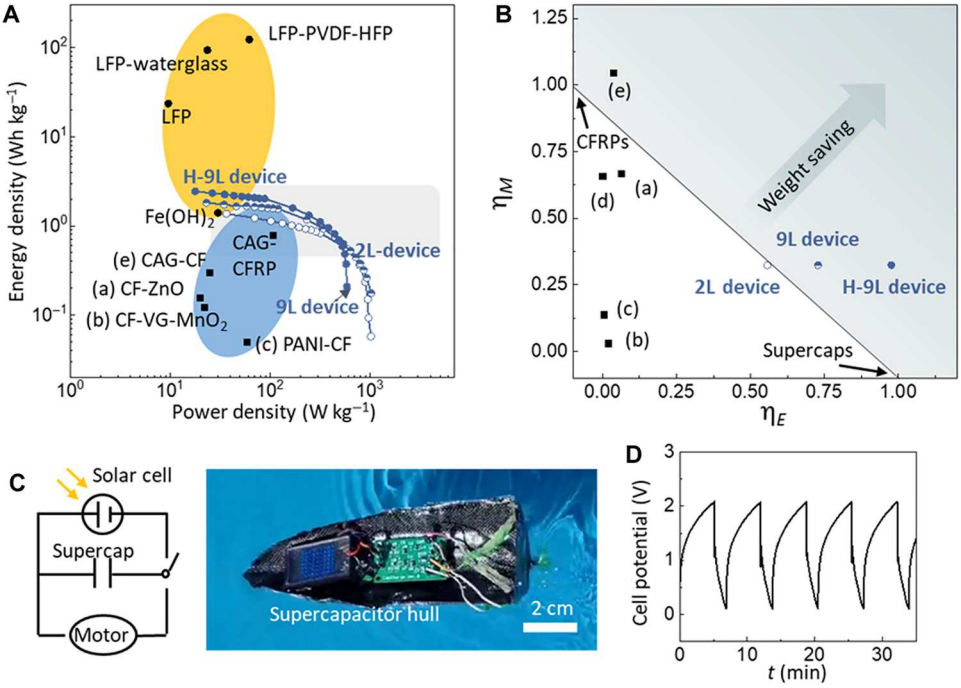

Fig. 5. Multifunctional efficiency of our structural supercapacitor. (**A**) Energy and power densities of structural energy storage devices. The shaded ovals categorize the devices into batteries (orange) and supercapacitors (blue). Our devices include a two-layer (2L) structure, a nine-layer (9L) structure, and a high-loading (H-9L) structure. The light gray region represents the typical characteristics of monofunctional supercapacitors that cannot provide structural functions. Structural batteries: $Fe(OH)_2$ (*35*), $LiFePO_4$ (LFP) (*17*), LPF-waterglass (*52*), and LFP-PVDF-HFP (*53*). Structural supercapacitors: (a) CF-ZnO (*14*), (b) CF-vertical graphene (VG)–MnO_2 (*54*), (c) PANI-CF (*55*), (d) graphene-CF (*56*) (0.07 mWh kg^{-1}, very small and thus not in the axis range), and (e) carbon aerogel (CAG)–CF (*57*). CAG–CF reinforced polymer (CFRP) (*58*), for which mechanical data are not available. (**B**) Multifunctional efficiency of state-of-the-art structural supercapacitors. Letter labels correspond to (A). Here, η_E is the energy density ratio and η_M is the tensile strength ratio compared to monofunctional structures. (**C**) A schematic and photograph of a boat model, in which the entire boat hull is a structural supercapacitor. The structural supercapacitor was charged by solar cells to power the boat motor as shown in the movie S1. (**D**) Charging/discharging voltage at the supercapacitor terminals versus time when operating within the energy-harvesting system to drive the boat motor.

Last, this work demonstrated the feasibility and benefits of using structural supercapacitors in a prototype boat. The structural supercapacitors were molded as a boat hull that realized weight and space savings and carried the entire energy-harvesting system. The hull stored the energy harvested by the on-board solar cell and in turn powered the boat motor. This autonomous system showed the utility of structural supercapacitors to serve as energy reservoirs for renewable energy sources. Here, the high-performance structural supercapacitors can extend the energy capacity to make electrified vehicles more compact and extend the operational time of electronics, adding a promising approach towards the goal of energy sustainability.

Experimental procedures

Electrode fabrication

The detailed synthesis and characterization of QxTh monomer was published in our previous work (*22*). The rGO powder was synthesized by a reduction process of GO solution with Zn powder in acidic condition (*39*). A solution of QxTh monomer (5 mg ml^{-1}) (*22*) and rGO (2 mg ml^{-1}) in CH_2Cl_2 was mixed in a sonicator for 2 hours. Then, the solution was drop casted onto a CF fabric (plain weave 1 K, 10.5 mg cm^{-2}, Toray T300, vendor Composite Envisions Inc.). The CF fabric was used as the working electrode in a three-electrode setup with 0.5 M $TEABF_4$ in propylene carbonate as the electrolyte. Meanwhile, the counter electrode was an active carbon (AC) electrode [mass ratio of AC (Kuraray, YP50F):polyinylidene fluoride (PVDF; Solvay PVDF 5130, M_w = 1300 kDa):carbon black (MTI, Super P conductive carbon black) was 7:2:1, with AC loading of ~4 mg cm^{-2}] coated on carbon cloth substrate. The reference was an Ag/Ag^+ electrode. A constant current of 0.25 mA cm^{-2} was applied to the CF fabric to conduct the electro-polymerization process until the working electrode reached 1 V versus Ag/Ag^+ reference, typically depositing 3 mg of QxTh-rGO coating on the 1-cm^2 electrode in roughly 1 hour at room temperature. The prepared QxTh-rGO@CF electrodes were annealed at 200°C for 30 min in inert nitrogen atmosphere. Following the same procedure as above for a single-sided coating, the QxTh-rGO solution could be drop cast on the flip side of the CF fabric, and the same electro-polymerization process was applied to prepare double-sided QxTh-rGO@CF electrodes.

Solid polymer electrolyte preparation

All the chemicals were used as purchased from Sigma-Aldrich. The solutions of $TEABF_4$ (2 M dissolved in propylene carbonate PC), PEO [molecular weight of 400,000 dissolved in acetonitrile (ACN) with a 1:15 weight ratio], and epoxy without the hardener–part A (Dow two-part epoxy, part 4001, extra-fast set epoxy, Hardman) were blended according to the ratios denoted in Fig. 3A. Before usage, the epoxy hardener–part B was added at 1:1 ratio with the epoxy and then thoroughly mixed. As a specific example, an electrolyte of 20-mg $TEABF_4$:40-mg PEO:320-mg epoxy (green circle in

Fig. 3A) was prepared as follows: (i) mix 50 μl of 2 M $TEABF_4$ in PC and 600 mg of the solution of PEO in ACN (equivalent to 40-mg PEO after ACN evaporated) and stir for 10 min to obtain a uniform, transparent solution; (ii) add 160-mg epoxy part A, which greatly increases the solution viscosity, and stir until the gel is uniform; (iii) add 160-mg epoxy hardener part B and stir to remove solvent. As solvent is removed, the gel should be used within an hour for stencil printing the electrolyte onto the electrodes or separators.

Structural supercapacitor fabrication

Structural supercapacitors were fabricated with QxTh-rGO@CF electrode. To match the capacitance of cathode and anode, the cathode was loaded with the redox materials at 1.5 times of the anode. The gradient and uniform electrolytes were fabricated with the same method as follows. The selected electrolyte was stencil printed on one side of the cathode, anode, and the cellulose separator (30 μm thick, NKK TF4030, Nippon Kodoshi Corporation), then placed under a vacuum for the electrolyte to vaporize its solvent and partially cure at 70°C for 1 hour. Then, the three components were stacked together and heat pressed together at 70°C and cured for 2 hours at 70°C. Afterward, the structural supercapacitor was sealed by laminating polyethylene terephthalate (PET) films (Sinopuren, TLP9IN3M100P) with heat laminator (Akiles, prolam photo) at 110°C to protect QxTh polymer and structural electrolyte from oxygen and moisture in atmosphere. The electrical connections were copper wires attached by conductive tape onto the electrode and then sealed by epoxy (Dow part 4001, extra-fast set epoxy, Hardman).

For the fabrication of the 9L and H-9L structural supercapacitors, the electrodes included two single-sided cathodes, three double-sided cathodes, and four double-sided anodes (fig. S10). The total capacitances of the cathode and anode electrodes were made to match for balancing materials utilization. Before assembly, the electrodes were held at −0.5 V for 1 min to keep at a neutral state. The electrolytes were stencil printed on both sides of the electrodes [using type (iii) electrolyte in Fig. 3A] and the cellulose separators [with type (ii) electrolyte], then placed under vacuum to evaporate solvent and partially cured at 70°C for 1 hour. Then, the device was assembled with following sequence: cathode-anode...cathode, where single-sided cathodes were used as the bottom and top layers of the device, while double-sided electrodes were in between. Separators were put between every pair of cathode-anode. In this stacking configuration, eight pairs of cathode-anode were achieved with only nine layers of CFs, thus saving the mass and volume of seven carbon-fiber layers compared to 8× 2L cells, which would use 16 layers of CF.

Materials morphology characterization

An FEI SEM at 5 kV was used for capturing materials morphology.

Electrochemical characterization

Electrochemical measurements were carried out via a BioLogic SP-200 potentiostat. The electrochemical measurements were repeated at least three times, and the uncertainty of the reported results was less than 5% of the reported mean values. For the electrodes alone, they were tested in the three-electrode Swagelok cell configuration, with AC on carbon cloth (AC loading ~4 mg cm^{-2}) as the counter electrode, Ag/Ag^+ as the reference electrode, and 0.5 M $TEABF_4$ in PC as electrolyte. The electrode measurements were conducted inside a glovebox with an inert N_2 atmosphere. The ionic conductivities of different electrolytes were inferred from electrochemical impedance spectroscopy performed at 0 V with an amplitude of 10 mV and frequencies ranging from 1 MHz to 100 mHz. The equivalent series resistance of the electrolyte samples were used to calculate ionic conductivity.

For the supercapacitors, they were encapsulated and measured in ambient. The capacitance C was calculated from CV characteristics based on the following equation (*40*).

$$C = \frac{1}{\Delta V \nu}\int_{V_1}^{V_2} i\, dV$$

Here, V_1 and V_2 are the starting and ending potentials in the discharge portion of the measurement, i is the current at each potential, $\Delta V = V_2 - V_1$ is the potential window, and ν is the voltage scan rate. The calculated capacitance was an average value across the whole potential window.

The capacity, power, and energy densities were calculated on the basis of following equations (*40*) using galvano-static charge-discharge (GCD) characteristics

$$\text{Capacity} = I \times t_d / M$$

$$E = \frac{I}{M}\int_0^{t_d} V dt$$

$$P = \frac{E}{t_d}$$

Here, I is the constant discharge current, t_d is the time interval of the GCD discharge period, E is the energy density, V is the measured potential, P is the power density, and M is the mass of electrode materials (QxTh-rGO-CF) in Fig. 3, whereas in Fig. 4, M is the total mass of the structural supercapacitor, including electrodes, separator, and electrolyte (but not including the encapsulation epoxy or PET films). The masses used for gravimetric calculations are listed in Table 2 below.

Mechanical strength measurement

Measurements of tensile stress versus strain and flexural stress under a three-point bending setup were conducted with an Instron 3369 universal testing machine equipped with a 1.0-kN load cell. The loading rate was 1 mm min^{-1} for the tensile test and 0.5 mm min^{-1} for the three-point bending test. Commercial grade paper Trimmer (Dahle, 18e) was used to cut CFs and separators into the target size. For tensile test on electrodes, CF fabrics were cut into 5 cm by 2 cm rectangular shape, with thickness of ~0.58 mm. The length, width, and thickness for mechanical properties calculation of each sample was measured with micrometer (±1 μm) before the test. Then, both ends (1 cm by 2 cm) were encapsulated by bonding them to carbon-fiber reinforced polymer (3 cm by 2 cm) with epoxy, to prepare the regions for clamping to the load cell. The final defined test area was a 3 cm by 2 cm rectangle. For the tests in Fig. 4, all the samples were cut to 10 cm by 1 cm rectangles, and then their two ends were also encapsulated by the same procedure as above. For the in situ mechanical-electrochemical measurements, CV sweeps were recorded for every 0.5-mm deflection to track the capacitance under mechanical loads. We note that the tensile stress was relatively constant under 0 to 0.5% strain in

Table 2. Specific masses and dimensions of electrodes and devices used for calculations of gravimetric capacitance and energy/power densities.

	Component masses	Dimensions	Notes
Fig. 2 (C to F)	CF: 9.9 mg; loading of QxTh-rGO showed in table S1.	All are round samples with 1 cm diameter	Gravimetric capacitance accounted for weights of both CF substrate and redox active materials
Fig. 3 (E to G)	Cathode: 15.57 mg (CF with 3-mg QxTh-rGO); anode: 14.32 mg (CF with 2-mg QxTh-rGO); cellulose separator: 1.02-mg electrolyte: PEO = 35.8 mg, uniform = 46.8 mg, gradient = 45.12 mg	Area of 1 cm by 1 cm	Calculations of gravimetric capacitance and energy/power densities included all components of electrodes, separator, and electrolyte conductive tape as contact leads; sealed by PET film
Fig. 4 (D and E)	Electrodes: QxTh-rGO (4.5 mg cathode and 3 mg anode) on 2 CF pieces (together 36.06 mg); cellulose separator: 1.97 mg; gradient electrolytes: 75.48 mg	Capacitor area of 1 cm by 1.5 cm, with the thickness roughly about 0.58 mm	Samples sealed by PET films
Fig. 5 (A and B)	9L device: for each CF layer, QxTh-rGO loading is 2.7 mg on each side of cathode; 1.9 mg on each side of anode; 12.6 mg for each CF piece; H-9L device: for each CF layer, QxTh-rGO loading is 6.2 mg on each side of cathode; 4.1 mg on each side of anode; total mass of devices: 2L device, 75 mg; 9L device: 343 mg (2× 15.3-mg single-sided cathode + 3× 18-mg double-sided cathode + 4× 16.3-mg double-sided anode; 8× 1.02-mg separators; gradient electrolyte = 185 mg); H-9L device: 435 mg (2× 18.8 mg for single-sided cathode + 3× 25 mg for double-sided cathode + 4× 20.8-mg double-sided anode, 8× 1.02-mg separators; gradient electrolyte: 232 mg)	Area of 1 cm by 1 cm	Conductive tape as contact leads; sealed by PET film
Fig. 5D	Boat prototype: 2.72 F structural supercapacitor, 2L configuration = 25.1 g, not including encapsulation	Boat length around 15 cm	Encapsulation: 11 g; solar cell: 3 V, 20 mA; motor: 3.7 V, 30,000 rpm

Fig. 4A. The samples were slightly twisted when placed in the sample holder, and unfortunately, we were not able to remove this artifact. Then, when tensile tests began, the applied tensile force was initially engaged in rearranging the sample in the sample holder, and this resulted in a constant stress output in the 0 to 0.5% strain region. Nonetheless, this would not affect the modulus value extracted from the slope of stress-strain characteristics (*41*).

The tensile stress σ and Young′s modulus G were extracted according to the following equation

$$\sigma = \frac{F}{d}$$

$$G = \frac{\nabla\sigma}{\nabla\varepsilon}$$

where F is the tensile force applied to the specimens, d is the thickness of the specimen, and $\nabla\sigma$ and $\nabla\varepsilon$ are changes in the tensile stress and tensile strain, respectively, in the linear region.

The flexural stress σ_f were calculated according to the following equation

$$\sigma_f = \frac{3FL}{2bd^2}$$

where F is the deflection force, L is the support span, and b and d are the width and thickness of the specimen, respectively.

Boat prototype fabrication and operation

For our model boat prototype, the boat hull was fabricated from a laminate of partially cured structural supercapacitor, prepared by pressing together the electrodes and cellulose separator coated with electrolyte resins for bonding. The hull was encapsulated by sandwiching it between two pieces of carbon aerogel–CF reinforced polymer (CFRP) and bonded to the hull by a layer of epoxy (fig. S11). A vacuum bag (Weavac, closure type: zipper, commercial grade) was used to shape the boat and degas the infusion epoxy. After curing overnight at room temperature, boat hull was released from the vacuum bag. The partially cured laminate was pressed against a mold to shape the workpiece into a hull form, and it was left in vacuum overnight to remove residual solvents. Afterward, it was annealed at 70°C for another 2 hours, and the fully cured structural supercapacitor hull was released from the mold. The boat hull was connected to the leads of the control circuit by copper wires attached with silver conductive tape. The control circuit was soldered to a solar cell (3-V 20-mA output, Sundance Solar Products) and a DC coreless motor (3.7 V, 30,000 rpm, XYDA0015N, Augiimor Inc.). The circuit components were placed inside the boat hull, while the motor shaft was mounted to the bottom of the boat on the CFRP encapsulation for driving the propeller outside the boat hull.

We designed a finite-state machine (FSM) circuit to control the logic of the system. The FSM had two states: 0, charging and 1, discharging. The FSM was implemented using simple discrete logic gates and flip-flops (figs. S12 and S13). A 32.768-kHz crystal oscillator (ECS-327) was used to provide clock for the digital circuit. Upon power on, the circuit initialized with state 0, the transistor PMOS U1 (IRLML2246) between the solar panel and the supercapacitor was turned on, and the charging process began. A comparator (LMV7271) was used to compare the supercapacitor voltage v_cap with the charging threshold voltage v_high and sent a charge-done signal when v_cap > v_high. When charge-done

signal was high, the circuit switches to state-1 upon the next rising edge of the clock. Consequently, the transistor NMOS U2 (IRLML6346) between the supercapacitor and the motor was turned on, U1 was turned off, and the discharging process began. Similarly, another comparator compared the v_cap with the discharging threshold v_low and sent a discharge-done signal when v_cap < v_low. The circuit would switch back to state-0 in the next clock cycle, and the process continued so on and so forth unless the circuit was switched off.

Supplementary Materials

This PDF file includes:
Figs. S1 to S13
Tables S1 to S4
References

Other Supplementary Material for this manuscript includes the following:
Movies S1 and S2

REFERENCES AND NOTES

1. Y. Zhou, H. Qi, J. Yang, Z. Bo, F. Huang, M. S. Islam, X. Lu, L. Dai, R. Amal, C. H. Wang, Z. Han, Two-birds-one-stone: Multifunctional supercapacitors beyond traditional energy storage. *Energ. Environ. Sci.* **14**, 1854–1896 (2021).
2. H. Zhou, H. Li, L. Li, T. Liu, G. Chen, Y. Zhu, L. Zhou, H. Huang, Structural composite energy storage devices — A review. *Mater. Today Energy* **24**, 100924 (2022).
3. Y. Xu, W. Lu, G. Xu, T.-W. Chou, Structural supercapacitor composites: A review. *Compos. Sci. Technol.* **204**, 108636 (2021).
4. L. E. Asp, M. Johansson, G. Lindbergh, J. Xu, D. Zenkert, Structural battery composites: A review. *Funct. Compos. Struct.* **1**, 042001 (2019).
5. J. L. Lutkenhaus, P. Flouda, Structural batteries take a load off. *Sci. Robot.* **5**, eabd7026 (2020).
6. B. J. Hopkins, J. W. Long, D. R. Rolison, J. F. Parker, High-performance structural batteries. *Joule* **4**, 2240–2243 (2020).
7. H. Wang, Y. Diao, Y. Lu, H. Yang, Q. Zhou, K. Chrulski, J. M. D'Arcy, Energy storing bricks for stationary PEDOT supercapacitors. *Nat. Commun.* **11**, 3882 (2020).
8. W. Johannisson, D. Zenkert, G. Lindbergh, Model of a structural battery and its potential for system level mass savings. *Multifunct. Mater.* **2**, 35002 (2019).
9. C. E. Jones, P. J. Norman, G. M. Burt, C. Hill, G. Allegri, J. M. Yon, I. Hamerton, R. S. Trask, A route to sustainable aviation: A roadmap for the realization of aircraft components with electrical and structural multifunctionality. *IEEE Trans. Transp. Electrif.* **7**, 3032–3049 (2021).
10. B. K. Deka, A. Hazarika, J. Kim, Y.-B. Park, H. W. Park, Recent development and challenges of multifunctional structural supercapacitors for automotive industries. *Int. J. Energy Res.* **41**, 1397–1411 (2017).
11. F. Rubino, A. Nisticò, F. Tucci, P. Carlone, Marine application of fiber reinforced composites: A review. *J. Mar. Sci. Eng.* **8**, 26 (2020).
12. Y. Chen, A. Amiri, J. G. Boyd, M. Naraghi, Promising trade-offs between energy storage and load bearing in carbon nanofibers as structural energy storage devices. *Adv. Funct. Mater.* **29**, 1901425 (2019).
13. H. Qian, A. R. Kucernak, E. S. Greenhalgh, A. Bismarck, M. S. P. Shaffer, Multifunctional structural supercapacitor composites based on carbon aerogel modified high performance carbon fiber fabric. *ACS Appl. Mater. Interfaces* **5**, 6113–6122 (2013).
14. B. K. Deka, A. Hazarika, O. Kwon, D. Kim, Y.-B. Park, H. W. Park, Multifunctional enhancement of woven carbon fiber/ZnO nanotube-based structural supercapacitor and polyester resin-domain solid-polymer electrolytes. *Chem. Eng. J.* **325**, 672–680 (2017).
15. K. Lee, Y. Shang, V. A. Bobrin, R. Kuchel, D. Kundu, N. Corrigan, C. Boyer, 3D printing nanostructured solid polymer electrolytes with high modulus and conductivity. *Adv. Mater.* **34**, 2204816 (2022).
16. R. Reece, C. Lekakou, P. A. Smith, A structural supercapacitor based on activated carbon fabric and a solid electrolyte. *Mater. Sci. Technol.* **35**, 368–375 (2019).
17. L. E. Asp, K. Bouton, D. Carlstedt, S. Duan, R. Harnden, W. Johannisson, M. Johansen, M. K. G. Johansson, G. Lindbergh, F. Liu, K. Peuvot, L. M. Schneider, J. Xu, D. Zenkert, A structural battery and its multifunctional performance. *Adv. Energy Sustain. Res* **2**, 2000093 (2021).
18. A. Javaid, K. K. C. Ho, A. Bismarck, J. H. G. Steinke, M. S. P. Shaffer, E. S. Greenhalgh, Improving the multifunctional behaviour of structural supercapacitors by incorporating chemically activated carbon fibres and mesoporous silica particles as reinforcement. *J. Compos. Mater.* **52**, 3085–3097 (2018).
19. S. J. Kwon, T. Kim, B. M. Jung, S. B. Lee, U. H. Choi, Multifunctional epoxy-based solid polymer electrolytes for solid-state supercapacitors. *ACS Appl. Mater. Interfaces* **10**, 35108–35117 (2018).
20. L.-Z. Fan, H. He, C.-W. Nan, Tailoring inorganic–Polymer composites for the mass production of solid-state batteries. *Nature Reviews Materials.* **6**, 1003–1019 (2021).
21. Y. Zheng, Y. Yao, J. Ou, M. Li, D. Luo, H. Dou, Z. Li, K. Amine, A. Yu, Z. Chen, A review of composite solid-state electrolytes for lithium batteries: Fundamentals, key materials and advanced structures. *Chem. Soc. Rev.* **49**, 8790–8839 (2020).
22. L. Yao, J. Liu, N. Eedugurala, P. Mahalingavelar, D. J. Adams, K. Wang, K. S. Mayer, J. D. Azoulay, T. N. Ng, Ultrafast high-energy micro-supercapacitors based on open-shell polymer-graphene composites. *Cell Rep. Phys. Sci.* **3**, 100792 (2022).
23. K. Wang, L. Huang, N. Eedugurala, S. Zhang, M. A. Sabuj, N. Rai, X. Gu, J. D. Azoulay, T. N. Ng, Wide potential window supercapacitors using open-shell donor–acceptor conjugated polymers with stable N-doped states. *Adv. Energy Mater.* **9**, 1902806 (2019).
24. S. E. Root, S. Savagatrup, A. D. Printz, D. Rodriquez, D. J. Lipomi, Mechanical properties of organic semiconductors for stretchable, highly flexible, and mechanically robust electronics. *Chem. Rev.* **117**, 6467–6499 (2017).
25. Q. Zhao, S. Stalin, C.-Z. Zhao, L. A. Archer, Designing solid-state electrolytes for safe, energy-dense batteries. *Nat. Rev. Mater.* **5**, 229–252 (2020).
26. H. Chen, M. Ling, L. Hencz, H. Y. Ling, G. Li, Z. Lin, G. Liu, S. Zhang, Exploring chemical, mechanical, and electrical functionalities of binders for advanced energy-storage devices. *Chem. Rev.* **118**, 8936–8982 (2018).
27. V. Augustyn, P. Simon, B. Dunn, Pseudocapacitive oxide materials for high-rate electrochemical energy storage. *Energ. Environ. Sci.* **7**, 1597–1614 (2014).
28. P. Simon, Y. Gogotsi, B. Dunn, Where do batteries end and supercapacitors begin? *Science* **343**, 1210–1211 (2014).
29. T. Brousse, D. Bélanger, J. W. Long, To be or not to be pseudocapacitive? *J. Electrochem. Soc.* **162**, A5185–A5189 (2015).
30. L. L. Lu, Y. Y. Lu, Z. X. Zhu, J. X. Shao, H. Bin Yao, S. Wang, T. W. Zhang, Y. Ni, X. X. Wang, S. H. Yu, Extremely fast-charging lithium ion battery enabled by dual-gradient structure design. *Sci. Adv.* **8**, eabm6624 (2022).
31. K. Wang, L. Yao, M. Jahon, J. Liu, M. Gonzalez, P. Liu, V. Leung, X. Zhang, T. N. Ng, Ion-exchange separators suppressing self-discharge in polymeric supercapacitors. *ACS Energy Lett.* **5**, 3276–3284 (2020).
32. Q. Zhang, J. Rong, D. Ma, B. Wei, The governing self-discharge processes in activated carbon fabric-based supercapacitors with different organic electrolytes. *Energ. Environ. Sci.* **4**, 2152–2159 (2011).
33. R. Reece, C. Lekakou, P. A. Smith, R. Grilli, C. Trapalis, Sulphur-linked graphitic and graphene oxide platelet-based electrodes for electrochemical double layer capacitors. *J. Alloys Compd.* **792**, 582–593 (2019).
34. R. Reece, C. Lekakou, P. A. Smith, A high-performance structural supercapacitor. *ACS Appl. Mater. Interfaces* **12**, 25683–25692 (2020).
35. C. Meng, N. Muralidharan, E. Teblum, K. E. Moyer, G. D. Nessim, C. L. Pint, Multifunctional structural ultrabattery composite. *Nano Lett.* **18**, 7761–7768 (2018).
36. D. J. O'Brien, D. M. Baechle, E. D. Wetzel, Design and performance of multifunctional structural composite capacitors. *J. Compos. Mater.* **45**, 2797–2809 (2011).
37. A. G. Patel, L. Johnson, R. Arroyave, J. L. Lutkenhaus, Design of multifunctional supercapacitor electrodes using an informatics approach. *Mol. Syst. Des. Eng.* **4**, 654–663 (2019).
38. W. Johannisson, S. Nguyen, G. Lindbergh, D. Zenkert, E. S. Greenhalgh, M. S. P. Shaffer, A. R. J. Kucernak, A residual performance methodology to evaluate multifunctional systems. *Multifunct. Mater.* **3**, 25002 (2020).
39. P. Liu, Y. Huang, L. Wang, A facile synthesis of reduced graphene oxide with Zn powder under acidic condition. *Mater. Lett.* **91**, 125–128 (2013).
40. T. S. Mathis, N. Kurra, X. Wang, D. Pinto, P. Simon, Y. Gogotsi, Energy storage data reporting in perspective—Guidelines for interpreting the performance of electrochemical energy storage systems. *Adv. Energy Mater.* **9**, 1902007 (2019).
41. G.-H. Dong, Y.-Q. Mao, G.-M. Yang, Y.-Q. Li, S.-F. Song, C.-H. Xu, P. Huang, N. Hu, S.-Y. Fu, High-strength poly(ethylene oxide) composite electrolyte reinforced with glass fiber and ceramic electrolyte simultaneously for structural energy storage. *ACS Appl. Energy Mater.* **4**, 4038–4049 (2021).
42. S. R. Kwon, J. Harris, T. Zhou, D. Loufakis, J. G. Boyd, J. L. Lutkenhaus, Mechanically strong graphene/aramid nanofiber composite electrodes for structural energy and power. *ACS Nano* **11**, 6682–6690 (2017).

43. Q. Yin, H. Jia, G. Liu, Q. Ji, Tailoring the mechanical performance of carbon nanotubes buckypaper by aramid nanofibers towards robust and compact supercapacitor electrode. *Adv. Funct. Mater.* **32**, 2111177 (2022).
44. Q. Liu, A. Zhao, X. He, Q. Li, J. Sun, Z. Lei, Z.-H. Liu, Full-temperature all-solid-state $Ti_3C_2T_x$/Aramid fiber supercapacitor with optimal balance of capacitive performance and flexibility. *Adv. Funct. Mater.* **31**, 2010944 (2021).
45. W. Tian, A. VahidMohammadi, M. S. Reid, Z. Wang, L. Ouyang, J. Erlandsson, T. Pettersson, L. Wågberg, M. Beidaghi, M. M. Hamedi, Multifunctional nanocomposites with high strength and capacitance using 2D MXene and 1D nanocellulose. *Adv. Mater.* **31**, 1902977 (2019).
46. T. Zhou, C. Wu, Y. Wang, A. P. Tomsia, M. Li, E. Saiz, S. Fang, R. H. Baughman, L. Jiang, Q. Cheng, Super-tough MXene-functionalized graphene sheets. *Nat. Commun.* **11**, 2077 (2020).
47. B. K. Deka, A. Hazarika, J. Kim, N. Kim, H. E. Jeong, Y.-B. Park, H. W. Park, Bimetallic copper cobalt selenide nanowire-anchored woven carbon fiber-based structural supercapacitors. *Chem. Eng. J.* **355**, 551–559 (2019).
48. H. H. Rana, J. H. Park, G. S. Gund, H. S. Park, Highly conducting, extremely durable, phosphorylated cellulose-based ionogels for renewable flexible supercapacitors. *Energy Storage Mater.* **25**, 70–75 (2020).
49. D. Lee, Y. Song, Y. Song, S. J. Oh, U. H. Choi, J. Kim, Multi-foldable and environmentally stable all-solid-state supercapacitor based on hierarchical nano-canyon structured ionic-gel polymer electrolyte. *Adv. Funct. Mater.* **32**, 2109907 (2022).
50. A. S. Westover, J. W. Tian, S. Bernath, L. Oakes, R. Edwards, F. N. Shabab, S. Chatterjee, A. V. Anilkumar, C. L. Pint, A multifunctional load-bearing solid-state supercapacitor. *Nano Lett.* **14**, 3197–3202 (2014).
51. C. Choi, K. Robert, G. Whang, P. Roussel, C. Lethien, B. Dunn, Photopatternable hydroxide ion electrolyte for solid-state micro-supercapacitors. *Joule* **5**, 2466–2478 (2021).
52. A. Ransil, A. M. Belcher, Structural ceramic batteries using an earth-abundant inorganic waterglass binder. *Nat. Commun.* **12**, 6494 (2021).
53. T. Jin, Y. Ma, Z. Xiong, X. Fan, Y. Luo, Z. Hui, X. Chen, Y. Yang, Bioinspired, tree-root-like interfacial designs for structural batteries with enhanced mechanical properties. *Adv. Energy Mater.* **11**, 2100997 (2021).
54. Z. Sha, F. Huang, Y. Zhou, J. Zhang, S. Wu, J. Chen, S. A. Brown, S. Peng, Z. Han, C.-H. Wang, Synergies of vertical graphene and manganese dioxide in enhancing the energy density of carbon fibre-based structural supercapacitors. *Compos. Sci. Technol.* **201**, 108568 (2021).
55. A. Javaid, O. Khalid, A. Shakeel, S. Noreen, Multifunctional structural supercapacitors based on polyaniline deposited carbon fiber reinforced epoxy composites. *J. Energy Storage* **33**, 102168 (2021).
56. A. Ganguly, A. Karakassides, J. Benson, S. Hussain, P. Papakonstantinou, Multifunctional structural supercapacitor based on urea-activated graphene nanoflakes directly grown on carbon fiber electrodes. *ACS Appl. Energy Mater.* **3**, 4245–4254 (2020).
57. M. F. Pernice, G. Qi, E. Senokos, D. B. Anthony, S. Nguyen, M. Valkova, E. S. Greenhalgh, M. S. P. Shaffer, A. R. J. Kucernak, Mechanical, electrochemical and multifunctional performance of a CFRP/carbon aerogel structural supercapacitor and its corresponding monofunctional equivalents. *Multifunct. Mater.* **5**, 25002 (2022).
58. G. Qi, S. Nguyen, D. B. Anthony, A. R. J. Kucernak, M. S. P. Shaffer, E. S. Greenhalgh, The influence of fabrication parameters on the electrochemical performance of multifunctional structural supercapacitors. *Multifunct. Mater.* **4**, 34001 (2021).
59. Y. Xu, S. Pei, Y. Yan, L. Wang, G. Xu, S. Yarlagadda, T.-W. Chou, High-performance structural supercapacitors based on aligned discontinuous carbon fiber electrodes and solid polymer electrolytes. *ACS Appl. Mater. Interfaces* **13**, 11774–11782 (2021).
60. Y. Wang, X. Qiao, C. Zhang, X. Zhou, Development of structural supercapacitors with epoxy based adhesive polymer electrolyte. *J. Energy Storage* **26**, 100968 (2019).
61. Y. Ding, G. Qi, Q. Cui, J. Yang, B. Zhang, S. Du, High-performance multifunctional structural supercapacitors based on in situ and ex situ activated-carbon-coated carbon fiber electrodes. *Energy Fuel* **36**, 2171–2178 (2022).
62. B. K. Deka, A. Hazarika, M.-J. Kwak, D. C. Kim, A. P. Jaiswal, H. G. Lee, J. Seo, C. Jeong, J.-H. Jang, Y.-B. Park, H. W. Park, Triboelectric nanogenerator-integrated structural supercapacitor with in situ MXene-dispersed N-doped Zn–Cu selenide nanostructured woven carbon fiber for energy harvesting and storage. *Energy Stor. Mater.* **43**, 402–410 (2021).

Acknowledgments

Funding: L.Y., N.K., N.E., J.D.A., and T.N.N. are grateful for the support from NSF PFI-TT 2120103. T.N.N. also received support from the NSF award MCA 2120701. K.Z. and X.Z. are supported by NSF CNS-1901048. Part of this work was performed at the San Diego Nanotechnology Infrastructure of UCSD, which is supported by NSF ECCS-1542148. **Author contributions:** L.Y. carried out the electrochemical polymerization, device fabrication, and characterization. N.K. fabricated and characterized the multilayer devices. K.Z. and X.Z. designed the control circuit for the structural supercapacitor boat. N.E. and J.D.A. designed, synthesized, and analyzed the monomer. T.N.N. conceived the idea and supervised the project. **Competing interest:** The authors declare that they have no conflict of interest. **Data and materials availability:** All data needed to evaluate the conclusions in this paper are present in the paper and/or the Supplementary Materials. The data for this study have been deposited in the database Mendeley V1, doi: 10.17632/t82g2m8hp2.1

Submitted 3 February 2023
Accepted 16 May 2023
Published 23 June 2023
10.1126/sciadv.adh0069